

Article

Numerical Investigation of Flow Past Bio-Inspired Wavy Leading-Edge Cylinders

Paulo Henrique Ferreira ^{*}, Tiago Barbosa de Araújo , Eduardo Oliveira Carvalho, Lucas Dantas Fernandes and Rodrigo Costa Moura

Aeronautical Engineering Division, Instituto Tecnológico de Aeronáutica (ITA),
São José dos Campos 12228-900, SP, Brazil

* Correspondence: paulohf@ita.br

Abstract: A numerical investigation is proposed to explore the flow past a novel wavy circular cylinder as a passive flow control, whose shape is determined by a sinusoidal function applied to its leading edge line, similar to studies with wavy leading-edge airfoils. The latter are motivated by the wavy-shaped tubercles found in the flippers of humpback whales, which are believed to improve their maneuverability. Our attempt is, therefore, to assess the effects of leading-edge waviness now on a simpler and canonical geometry: circular cylinders. The present work relies on iLES simulations conducted with Nektar++ at a Reynolds number of 3900. Besides the straight cylinder, two wavy geometries are assessed, which are determined by a single wavelength of 37.5% for two amplitudes, 3% and 11%, based on the mean diameter of the wavy cylinder. Our results showed that, contrary to what is usually the case with traditional wavy cylinders at similar Reynolds numbers, waviness caused a reduction in the near-wake recirculation length and an increase in the mean near-wake turbulent kinetic energy compared to the straight cylinder. This was followed by a reduction in base pressure (up to about 36%) leading to a rise in lift oscillations and also to a significant increase in the mean drag coefficient of up to about 28%. An attempt to detail the flow phenomena is provided, evidencing the emergence of counter-rotating pairs of streamwise vortices between peaks. It is argued that the differences observed in recirculation length, turbulent kinetic energy, and force coefficients start even prior to the formation of these coherent structures and end up with interactions with the near wake.

Keywords: wavy cylinder; wavy leading-edge airfoil; spectral element method; continuous Galerkin method; implicit large-eddy simulation



Citation: Ferreira, P.H.; de Araújo, T.B.; Carvalho, E.O.; Fernandes, L.D.; Moura, R.C. Numerical Investigation of Flow Past Bio-Inspired Wavy Leading-Edge Cylinders. *Energies* **2022**, *15*, 8993. <https://doi.org/10.3390/en15238993>

Academic Editors: Artur Bartosik and Dariusz Asendrych

Received: 3 October 2022

Accepted: 21 November 2022

Published: 28 November 2022

Publisher's Note: MDPI stays neutral with regard to jurisdictional claims in published maps and institutional affiliations.



Copyright: © 2022 by the authors. Licensee MDPI, Basel, Switzerland. This article is an open access article distributed under the terms and conditions of the Creative Commons Attribution (CC BY) license (<https://creativecommons.org/licenses/by/4.0/>).

1. Introduction

Many researchers have exhaustively studied flow over bluff bodies, especially cylinders, such as Roshko [1], Williamson [2], and Zdravkovich [3]. Whether due to the simplicity of the geometry or the intriguing complexity of the emerging flow structures, cylinders have always aroused this interest over time. Additionally, this geometry has always been present in everyday life, in different engineering applications, e.g., flow over buildings, wind turbines, and oil risers, which reinforces its importance, especially by knowing they suffer the action of a phenomenon called vortex-induced vibration (VIV). In a simplified way, this is an oscillating effect induced by the interaction of pressure fluctuations created by a vortex-shedding wake on the body itself, which can even compromise its structural integrity [4].

In the search for solutions to mitigate or suppress phenomena such as VIV, or simply to reduce drag or the mean lift fluctuations (i.e., RMS of lift forces), many studies have been carried out with passive flow control mechanisms. In other words, those mechanisms do not have an active device, but work by changing the body geometry itself, e.g., a surface undulation, like the one that will be presented here, or the addition of some fixed external

structure to the body surface, such as the well-known vortex generator [5], that helps to improve stall characteristics.

Despite also having a circular cross-section, different from the planform of the typical existing wavy cylinders, the present work proposes a new bio-inspired planform cylinder, as shown in Figure 1, here named the “wavy leading-edge cylinder”. The inspiration comes from works on wavy leading-edge wings, whose study was first motivated by the morphological observations made by Fish and Battle [6], in 1995, about humpback whales. This study hypothesized that the presence of some protuberances (also called tubercles) almost regularly distributed on the leading-edge surface of the humpback whale flippers acted like a flow control mechanism responsible for the distinct hydrodynamic characteristics of these animals, which are known to be excellent hunters, and are able to perform complex movements with great ease and under high angles of attack.

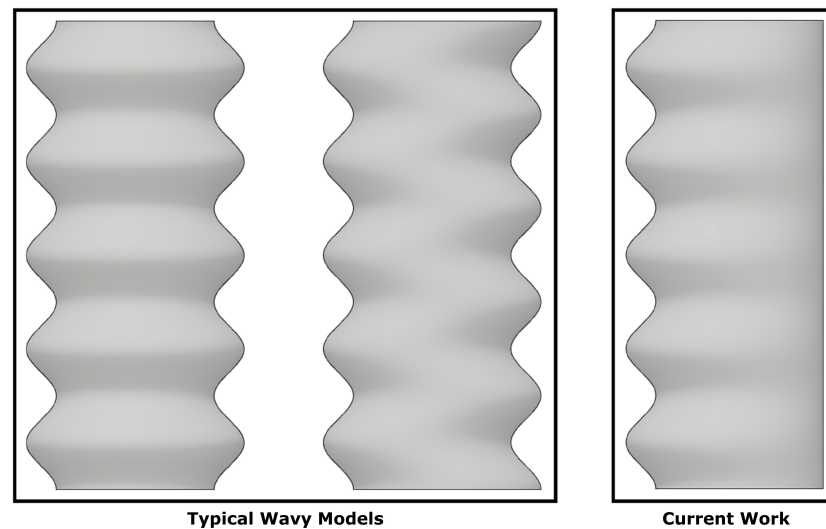


Figure 1. Types of wavy cylinders (in each cylinder, the leading edge appears on the left and the trailing edge on the right). The right-most cylinder shows the waviness adopted in the current work, whereas the other two cylinders show the typical patterns of waviness considered in the literature.

Different studies [7–12] mimicking those tubercles have tried to understand how this geometry allowed to improve maneuverability and whether they could enhance the aerodynamic performance of wings. Those studies have evidenced interesting phenomena and promising results, such as three-dimensional effects like the emergency of longitudinal counter-rotating vortex pairs (CVP), the formation of three-dimensional laminar separation bubbles (LSB), the delay of boundary layer detachment, a more evenly distributed surface pressure, an aerodynamic efficiency improvement (by reduction of drag and/or increase of lift), and so on.

After this brief overview of wavy leading-edge airfoils, we turn to the theme of this work. The proposed waviness modification was created by giving volume to a geometry after sweeping a circular area through a planform constrained by a sinusoidal function curve at the leading-edge line and a straight line at the trailing-edge line, as shown in Figure 2. This is a computational part of a research that also includes an experimental part [13] for the same geometries, but at higher Reynolds numbers. As will be discussed in the present work, the applied waviness resulted in a drag increase at the current (lower) Reynolds of 3900, showing there is also an important Reynolds effect at play.

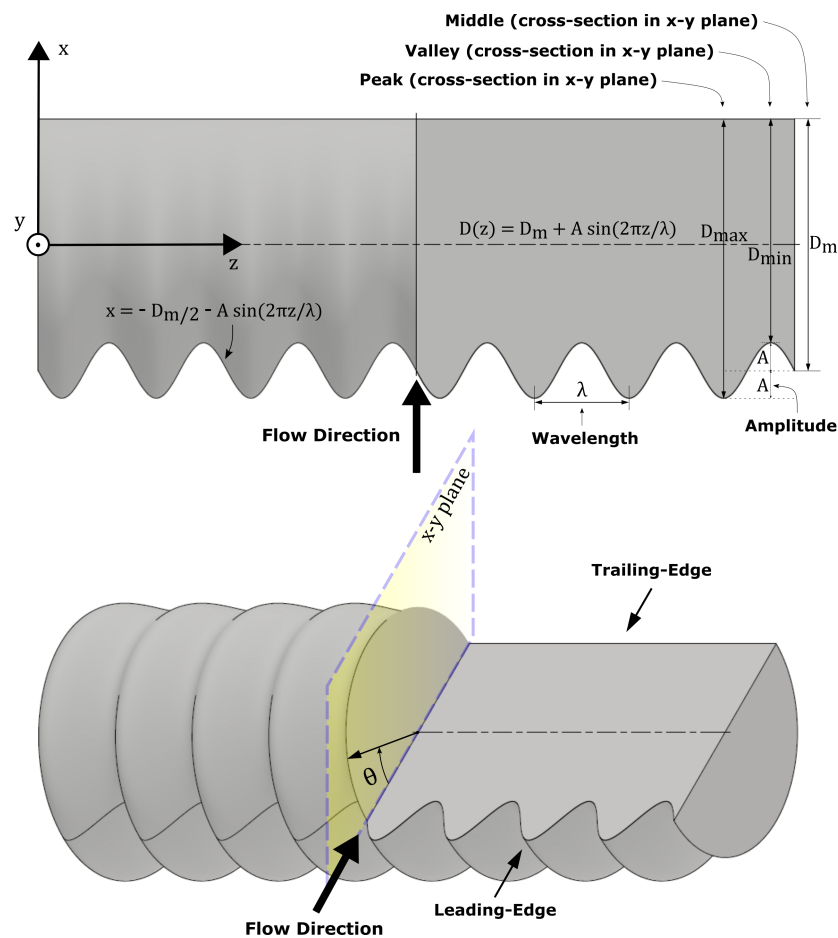


Figure 2. Sectional views—cutting plane (top) and three-dimensional view (bottom)—of the new flow control geometry proposed: the wavy leading-edge cylinder geometry. The illustrative figure presents the main parameters and constructive function in the x - z plane.

Here, simulations were conducted first to validate the numerical model for the straight cylinder at $Re = 3900$ and then to investigate two wavy geometries at the same Reynolds, namely two amplitudes for a single wavelength. At this Reynolds number, the straight cylinder is well within the subcritical regime, in which the boundary layer is laminar and transition occurs along the separating shear layer (via Kelvin–Helmholtz instability) leading to a turbulent wake featuring the well-known von-Kármán vortex street. In the near wake region, the interaction between the transitional shear layer and the wake creates three-dimensional turbulent structures that evolve in both streamwise and spanwise directions.

Focusing on wavy cylinders, Ahmed and Bays-Muchmore [14] were among the first authors to carry out experiments with transverse flow over a wavy cylinder. In this case, they measured surface pressure in a wind tunnel for a Reynolds number of 10,000 and performed dye visualizations in a water tunnel for Reynolds numbers of 5000, 10,000, and 20,000. They tested a traditional sinusoidal wavy planform with symmetric waviness in the spanwise direction for a set of wavy models with wavelength (λ) ratio to the mean diameter D_m of $\lambda/D_m = 1.2, 1.6, 2.0,$ and 2.4 , and a fixed amplitude ratio of $A/D_m = 0.1$. They found that waviness reduces overall drag and observed that the sectional (2D) drag coefficients were greater at peaks (larger diameter section) than at valleys (smaller diameter section). Additionally, they found that separation was anticipated on valleys and delayed on peaks. Note that the frontal pressure typically changes along the spanwise direction, also influencing differences in drag between sections. In addition, the separation line maintained a curvature proportional to the wavy geometry applied, following a wavy pattern. Additionally, from flow topology analysis, they inferred the possible formation of a pair of longitudinal vortices in between adjacent peaks.

Zhang et al. [15] carried out experiments in a water channel at a Reynolds number of 3000 in order to investigate the near wake behavior of a wavy cylinder through a particle image velocimetry (PIV) measurement technique. From the transverse vorticity results, they inferred the formation of structures supposed to be a pair of counter-rotating stream-wise vortices at both sides of each peak. These vortices showed an action to suppress the development of both large-scale spanwise vortices and regular vortex shedding. This effect indicated a possible reason for the reduction in the average turbulent kinetic energy (TKE) over the near-wake region, especially after the valley regions. Therefore, this consequential lower TKE also helped to justify lower values of drag coefficient compared to the straight cylinder.

Lam and Lin [16] conducted a large-eddy simulation (LES) to study the flow past wavy cylinders at a Reynolds number of 3000. They tested a combination of parameters for λ/D_m varying from 1.136 to 3.333, and two amplitude ratios, $A/D_m = 0.091$ and 0.152. The most notable result was a reduction of about 18% in drag when compared to the straight cylinder, for $\lambda/D_m = 1.9$ and $A/D_m = 0.152$. In addition, waviness caused a reduction or even a suppression of RMS lift coefficients with no significant changes in Strouhal number (St). Furthermore, they observed that waviness created a difficulty for the vortex sheet to roll up, which ended up moving downstream the vortex formation region. This three-dimensional free shear layer effect helped them to explain the less intense pressure fluctuations over the surface and the lower values of turbulent kinetic energy in the wake (compared to the “two-dimensional” wake of the straight cylinder), leading to higher base pressure values and lower drag coefficients.

Lin and Yu-fen [17] conducted a large-eddy simulation study, with an experimental validation of the straight model in a wind tunnel, to investigate the effect of waviness at a Reynolds number of 3000. They tested a single combination of wavelength and amplitude ratios, namely $\lambda/D_m = 1.5$ and $A/D_m = 0.15$. Their conclusions suggested that waviness imposed a difficulty for the formation of a vortex street, also with less intense pressure fluctuations and smaller values of turbulent kinetic energy over different spanwise cross-sections in the wake. Those effects led to a reduction in both mean drag and RMS lift coefficients. Again, the separation was anticipated in the valleys and delayed in the peaks.

Lam et al. [18] performed a large-eddy simulation and an experimental validation with laser Doppler anemometry (LDA) and load cell measurements in water and wind tunnels, to investigate flow past a yawed wavy cylinder at a Reynolds number of 3900. They tested a single combination of wavelength and amplitude ratios, $\lambda/D_m = 6.0$ and $A/D_m = 0.15$, respectively, with yaw angle varying from 0° to 60° . The results of the flow with yaw angle = 0° (or unyawed), which is the main interest for the present work, showed drag and RMS lift coefficients reductions of up to 14% and 80%, respectively. Power spectral density (PSD) revealed a lower St , namely 0.184 against 0.208 from the straight cylinder. Moreover, pressure and velocity distributions confirmed spanwise periodic and repetitive wake structures, following the pattern imposed by the wavy geometry.

Zhao et al. [19] implemented a scale-adaptive simulation to understand the physics of the flow past a wavy cylinder at Reynolds number 8000 for several configurations. They varied λ/D_m from 3 to 7 for $A/D_m = 0.091$ and 0.152. They confirmed results already obtained by other authors, with reductions in Cd , St , and Cl_{RMS} of up to 30%, 50%, and 92%, respectively, compared to the straight case. Besides associating the reduction of lift fluctuations to the presence of longitudinal vortices, they visualized for certain configurations a change in the pattern of surface streamlines after the separation line (curve). Lastly, they also observed longer mean recirculation lengths, which means spanwise vortex formation moved downstream, which led to a base pressure increase and corresponding drag reduction.

Bai et al. [20] investigated flow past wavy cylinders in a water tunnel at a Reynolds number of 3000 through a time-resolved PIV (TR-PIV) technique. They tested a single model of $\lambda/D_m = 0.152$ and $A/D_m = 6$. PSD results revealed two different vortex-shedding frequencies associated with peak and valleys sections, respectively, of $f = 0.164$ and

$f = 0.214$, the last one very close to the Strouhal number expected for a straight cylinder at this Reynolds number ($St = 0.21$), indicating that larger structures such as von-Kármán vortices still dominate flow. An analysis based on proper orthogonal decomposition (POD) in the spanwise direction corroborated this by showing that the first two dominant modes exhibit the spanwise vortex shedding in valleys and peaks and together concentrate almost 45% of the POD energy. Despite that, near the wake in the streamwise direction, the most energetic POD modes were associated with the presence of the streamwise vortices, which tend to suppress the coherence of spanwise vortices. In addition, they observed that mean recirculation lengths extend further downstream, more in peaks than in valleys, as well as when compared to the straight cylinder.

Karthik et al. [21] studied the flow past a wavy cylinder using LES along with the Ffowcs, Williams and Hawking's (FWH) acoustic analogy at Reynolds number 97,300. They tested all combinations of parameters for $\lambda/D_m = 1.0, 1.5, 2.0$, and 2.5 , and $A/D_m = 0.05, 0.1, 0.15$, and 0.2 . Drag and RMS lift reduced in all wavy cases, with the greatest drag reduction for $\lambda/D_m = 2.0$, and the minimum RMS lift for $\lambda/D_m = 1.5$, among all amplitudes. The parameters for the optimum case for both drag and sound emission were $\lambda/D_m = 1.892$ and $A/D_m = 0.134$, with a reduction of 33.21% and 6.331 dB compared to the straight case, respectively. They associated these results with a mean increase in base pressure distribution and a reduction in average vorticity in the near wake.

Finally, a recent relevant study was conducted by Zhang et al. [22], in which LES was used for the comparison of different models at Reynolds number 3900, namely for wavelength ratios varying from 1.8 to 5.0 and amplitude ratios from 0.05 to 0.2. They characterized flow structures developed in the wake as rib-like vortices and three-dimensional vortex lines caused by waviness along the span. Besides that, they also identified longitudinal vortices, and evidenced their similarities with some vortex generator mechanisms. Based on the analysis of two components of the transport equation for vorticity, namely stretching and turning terms, they inferred two vortex formations, which they called primary and secondary vortices. The primary seems to induce the secondary one. The first is dominant while the second tends to disappear with increasing wavelengths. A correlation between longer recirculation lengths and drag reduction is observed for all their wavy cylinders. Drag reduction was found for greater amplitudes and/or smaller wavelengths. Analysis of surface streamlines revealed a flow from the peak to valley before the separation line (curve). The pressure at the stagnation position (leading edge) at peaks and valleys is about the same as the straight cylinder, while the middle section presents a reduction in static pressure, especially for the models with largest amplitude.

Despite being a topic already explored in the literature, others wavy cylinders do not have the same inspiration as the present work. In addition to the geometric transformation applied by the undulation being different, the parameters (wavelength and amplitude) also differ from those typically selected in the wavy cylinder literature. In addition to the presentation of the results, an attempt is also made to establish a correlation that explains the emerging phenomena.

As will be seen later, even though the results were different from what was expected based on the wavy airfoils, since it is a recent and developing topic, the understanding of the phenomenon behind this bio-inspired waviness in a simpler and canonical geometry, such as the circular cylinder, may be useful for other authors to be able to better describe the flow over wavy airfoils or others wavy geometries.

Regarding the wavy cylinders already existing in the literature, it was not expected to find the same results, since they are similar geometries, but not the same, even so, apparently, the phenomenology appears to be common to both. Regarding a possible application of this new geometry, which has a preferential or fixed direction, we can mention rotary wings, such as those found in helicopters, and rotate blades in wind turbines.

This paper is organized as follows. In Section 2, the methodology of the study is presented along with the definition of the numerical domain, the description of the meshes employed and boundary conditions adopted. In Section 3, the numerical results are

presented and discussed, starting with a validation of the numerical method as per the results obtained for the straight cylinder, followed by a discussion of the main characteristics found for the wavy models and a detailed assessment of three-dimensional flow structures. Finally, Section 4 summarizes the conclusions of the study.

2. Materials and Methods

The present study made use of the high-fidelity implicit large-eddy simulation (iLES) approach based on spectral/hp element methods (SEM) [23]. Broadly speaking, this approach relies on numerical dissipation in lieu of a traditional turbulence model, no subgrid-scale model is employed, and has become very popular in recent decades. In this context, iLES has also been called under-resolved direct numerical simulation (uDNS) [24]. For a detailed study on why and how to use SEM-based iLES/uDNS, the reader is referred to references [25–36].

The SEM adopted was the high-order continuous Galerkin (CG) method coupled with a novel stabilization scheme particularly suited for the simulation of transitional and turbulent flows [37,38]. This technique is called gradient-jump penalty (GJP) and has even been proven superior to modern versions of the well-known spectral vanishing viscosity (SVV) operator [39]. Simulations were conducted with the Nektar++ open-source code [40,41], a mature platform that has been successfully employed multiple times for iLES/uDNS [42–45].

The adopted unsteady CG solver [46] is based on a spectral/hp element method that provides a continuous Galerkin projection as a linear combination of a set of a particular polynomial basis functions Φ_n , such that:

$$u^\delta = \sum_{n \in N} \Phi_n \hat{u}_n, \tag{1}$$

where \hat{u}_n are the coefficients of our solution vector $\hat{\mathbf{u}}$ to the approximate solution u^δ in the reduced finite-dimensional function space $U_\delta \subset U$ for a linear differential equation type:

$$\mathbf{L}(\mathbf{u}) = f, \tag{2}$$

which can be replaced by our incompressible Navier–Stokes equations to be solved, i.e.,

$$\frac{\partial \mathbf{u}}{\partial t} = \mathbf{N}(\mathbf{u}) - \nabla p + \nu \mathbf{L}(\mathbf{u}), \tag{3}$$

$$\nabla \cdot \mathbf{u} = 0, \tag{4}$$

where:

$$\mathbf{N}(\mathbf{u}) = -(\mathbf{u} \cdot \nabla) \mathbf{u}, \tag{5}$$

$$\nu \mathbf{L}(\mathbf{u}) = \nu \nabla^2 \mathbf{u}. \tag{6}$$

They are solved along with the appropriate boundary conditions described later on. The pressure is solved by the following velocity correction scheme:

$$\int_{\Omega} \nabla p^{n+1} \cdot \nabla \phi d\Omega = \int_{\Omega} \nabla \cdot \left(\frac{-\hat{\mathbf{u}}}{\Delta t} \right) d\Omega + \int_{\Gamma} \phi \left[\frac{\hat{\mathbf{u}} - \gamma_0 \hat{\mathbf{u}}^{n+1}}{\Delta t} - \nu (\nabla \times \nabla \times \mathbf{u})^* \right] \cdot \mathbf{n} dS, \tag{7}$$

where Ω is the domain and Γ is the boundary domain, with a backward approximation of the time derivative, such that:

$$\hat{\mathbf{u}} = \mathbf{u}^\oplus + \Delta t \mathbf{N}^*, \tag{8}$$

where $(*)$ denotes the time extrapolation, and (\oplus) the backward differencing. It uses a second-order implicit–explicit (IMEX) time-integration scheme. The velocity is the solution of the Helmholtz problem given by:

$$\frac{\gamma_0 \mathbf{u}^{n+1} - \hat{\mathbf{u}}}{\Delta t} = -\nabla p^{n+1} + \nu \mathbf{L}(\mathbf{u}^{n+1}). \quad (9)$$

2.1. Computational Domain and Baseline Mesh

The simulation domain is initially based on a two-dimensional mesh of quadrilaterals, as shown in Figure 3, which is then extruded along the spanwise direction in a way that allows for the desired waviness to be incorporated. The dimensions of the domain, i.e., the distances upstream and downstream of the body, the height and the width were based on dimensions previously established as sufficient to avoid blockage, with a blockage ratio (diameter/height) less than 3.4%, and allow the proper development of the wake [47,48].

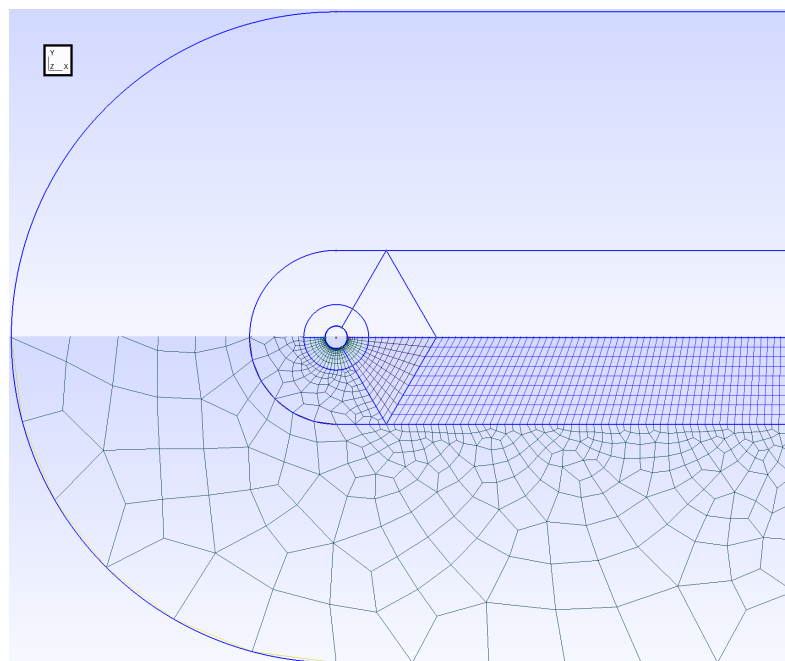


Figure 3. Two-dimensional mesh. It is worth noting that this mesh has not yet received p-type refinement ($N_p = 2$), that is, in this case, in each direction the elements still will be “divided” in half, then increasing its resolution.

Note the mesh is of a structured pattern around the cylinder and along the wake, whereas elsewhere it is of an unstructured pattern. In SEM, the solution inside each element is represented through a polynomial expansion. Here, the element-wise polynomial order has been chosen as $P = 2$ (parabolic solution per element). Note that CG’s nominal order of accuracy is $P + 1$, hence all the solutions presented here are nominally third-order accurate.

The circular cylinder is placed at the center of the domain (origin of Cartesian coordinates) and has a diameter D of unit size. The outermost boundary is made up of a semi-circle (inflow boundary of radius $15D$) and a rectangle whose downstream closure coincides with the outflow boundary (at $x \approx 21D$). The intermediate part of the mesh, as also shown in Figure 3, has another semi-circular section (of radius $4D$) that connects to two symmetric triangular sections. These exist as means for the mesh to transition into the wake region, which extends downstream until the outflow boundary.

Around the cylinder, there is an outer circle (of radius $1.5D$) and an inner circle (of radius $D/2 + \delta_{BL}$) placed very close to the cylinder’s surface, as shown in Figure 4. The latter

is devoted to capturing the (laminar) boundary layer of the simulation, whereby its thickness is adjusted based on the cylinder's Reynolds number Re_D according to the estimate

$$\delta_{BL} \approx D (Re_D)^{-1/2}, \quad (10)$$

which was found to approximately match the boundary layer thickness next to its separation point. This innermost circular layer is subdivided into 5 equispaced layers that are deemed sufficient to resolve the cylinder's laminar boundary layer, given the high-order nature of the elements within the equispaced layers. For example, when using $P = 2$ element-wise polynomials in the solution, the innermost circular region will have $2 \times 5 = 10$ DOF (degrees of freedom) across the radial direction.

It is also worth mentioning that, in terms of resolution power, a SEM-type DOF is somewhat superior to the DOF of classical CFD schemes, as can be seen in dispersion/diffusion analyses [25,27]. In fact, these considerations apply to all the elements in the domain, which is why the mesh in Figures 3 and 4 may seem too coarse for those unfamiliar with SEM. If the mesh was shown with "subelements" representing the element-wise polynomial DOFs, it would look much finer.

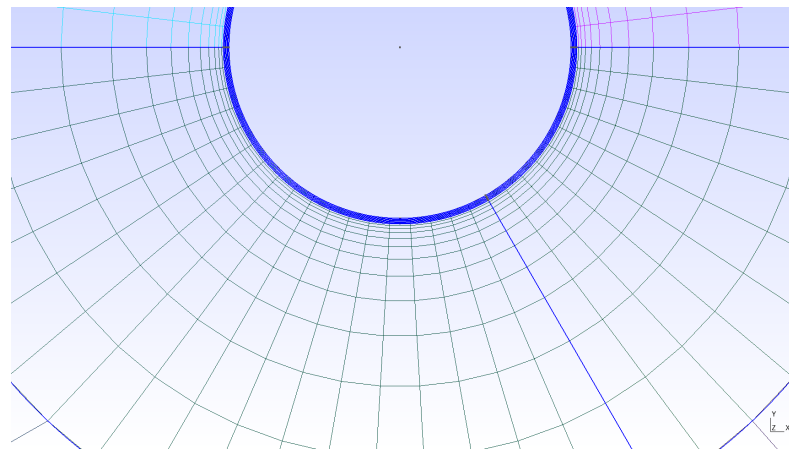


Figure 4. Close-up view of the mesh next to the cylinder. It is worth noting that this mesh has not yet received p-type refinement ($N_p = 2$), that is, in this case, in each direction the elements still will be "divided" in half, increasing their DOF.

From the edge of the boundary layer region, the radial mesh size grows geometrically toward the outer circle around the cylinder, when the radial mesh size achieves the same mesh spacing employed horizontally along the wake ($\approx 0.25D$). Along the cylinder's wall, in the azimuthal direction, 54 equispaced elements (or angular subdivisions) are used to cover the whole circle. This also defines the azimuthal size of the mesh along the outer circle, which in turn defines the vertical mesh size along the wake ($\approx 0.35D$).

As mentioned previously, the regions within the cylinder's outer circle, along with the two symmetric triangular regions plus the wake region follow a structured mesh pattern. The other regions of the domain have a mesh with an unstructured pattern. All meshes have been generated with GMSH [49], an open-source finite element mesh generator. A third-order mesh representation was used in all the cases, i.e., one order above the polynomial order adopted for the numerical solution near the surface, as per typical SEM guidelines for simulating flows around curved geometries.

2.2. Mesh Generation

The 2D mesh described in the previous section is the same for all the cases simulated. To obtain the actual three-dimensional meshes, the baseline 2D mesh is extruded along the spanwise direction over a distance $L_z = 3D$, which is typically found to be sufficiently large according to the literature. Waviness is then incorporated in the 3D mesh through a simple mapping transformation, which shifts mesh coordinates on the original surface

of the cylinder to the desired case-dependent wavy surface. The mapping is such that the original trailing edge is left untouched, whereas the leading edge becomes wavy according to a sine function of a given wavelength and amplitude (Figure 2). This transformation also shifts vertical mesh coordinates, so that any cross-section (normal to the spanwise direction) slicing the wavy cylinder marks an actual circle in its new surface, albeit one of variable diameter size.

To avoid invalid elements, the mapping intensity is made to decrease linearly with the radial distance, from the cylinder's surface to the outer circle in the intermediate mesh region, where the mapping intensity becomes zero. Hence, only the region within the cylinder's outer circle (recall Figure 3) is affected by the mapping. The mesh coordinates in GMSH's original file are then updated and Nektar++ is able to load it just as a normal GMSH file. A view of a mesh with 11% amplitude waviness is shown in Figure 5.

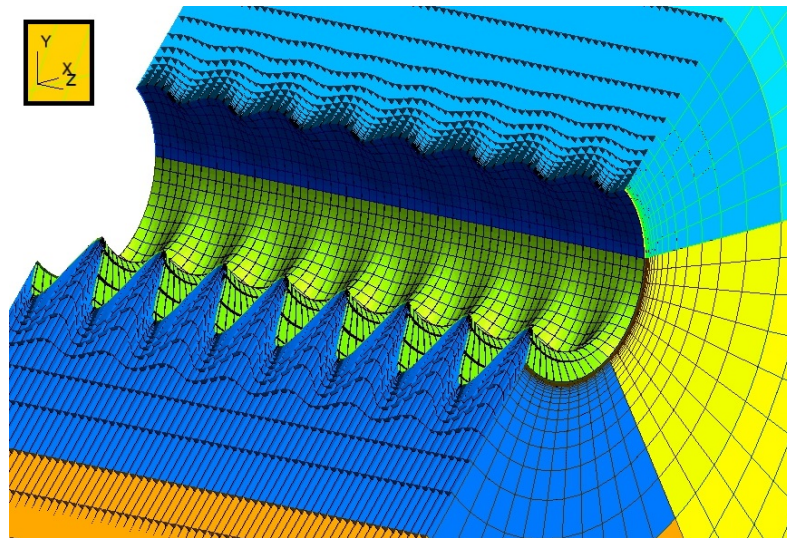


Figure 5. Cross-sectional view of a mesh showing the mapping pattern for $\lambda = 0.375D_m$, and waviness amplitude 11% (the line of contact between the green and dark blue regions is the cylinder's trailing edge).

2.3. Boundary and Initial Conditions

The following boundary conditions were imposed on the boundary surfaces shown in Figure 6:

- Viscous wall (no-slip and impermeability) conditions at the cylinder surface, along with Neumann condition for the pressure ($\partial p / \partial n = 0$, where n denotes the unit vector normal to the relevant surface);
- Periodic condition connecting the opposite surfaces in the spanwise direction (back and front planes in Figure 6);
- Dirichlet boundary condition for the velocity ($u = 1, v = 0, w = 0$) at the inlet surface, along with Neumann condition for the pressure ($\partial p / \partial n = 0$); these same conditions were applied for the outermost top and bottom domain surfaces shown in Figure 6;
- Nektar's high-order outflow boundary condition at the outlet surface, which enforces a Dirichlet condition for the pressure ($p = 0$) while allowing for velocity fluctuations across the outlet.

In order to facilitate the vortex shedding formation and, consequently, speed up the transient state, the following initial conditions given by simple arbitrary functions with respect to the domain coordinates were imposed:

$$u = 1.0 - \frac{0.1(x-1.0)}{(x-1.0)^2 + y^2 + 0.1}; v = \frac{0.1y}{(x-1.0)^2 + y^2 + 0.1}; w = 0; p = 0. \quad (11)$$

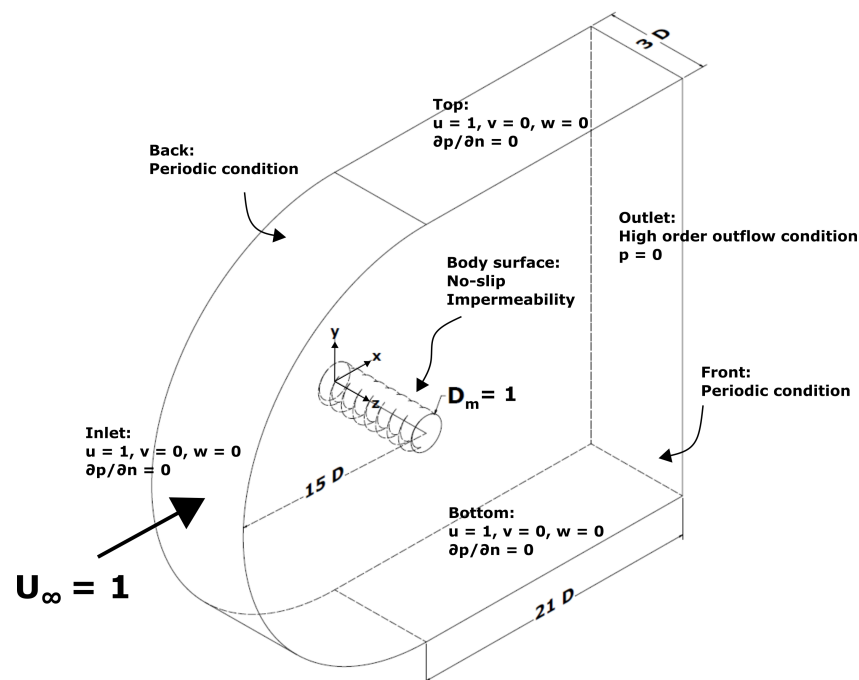


Figure 6. Computational domain (representative, not to scale) showing the surfaces on which boundary conditions are applied.

2.4. Simulation Details and Cases

Three cases have been simulated in the present work, including the straight model, as listed in Table 1. The two wavy models have the same wavelength, $\lambda/D = 0.375$, and undulation amplitudes of 3% and 11%. In all simulations, the initial $100 D/U_\infty$ time units were considered as numerical transient, in which the turbulent wake was left to accommodate across the domain. This time span corresponds to approximately 20 vortex shedding cycles and also allows for a number of large vortices to first leave the domain through the outlet boundary. The cases were then further simulated in order for the flow statistics to be collected, up to a total of $290 D/U_\infty$ time units for a good statistical convergence.

Table 1. Geometry parameters for the models simulated.

Case	Type	A/D_m	λ/D_m
Baseline	Straight	-	-
A03	Wavy	0.03	0.375
A11	Wavy	0.11	0.375

We note that, according to Lam and Lin [16], who performed LES of several wavy configurations, cases with smaller wavelengths end up requiring less time for statistics' convergence, provided $\lambda/D < 1$, due to the spanwise periodicity imparted on the wake structures (modulating the spanwise length of the largest wake structures). Therefore, the time required for the convergence of the wavy cases' statistics is expected to be less than that of the straight cylinder case.

To remind the reader, by keeping the same common position on the trailing-edge line, the cross section of the wavy cylinder is always a circle, and its diameter at any position along span (z coordinate) is given by:

$$D(z) = D_m + A \sin\left(\frac{2\pi z}{\lambda}\right), \quad (12)$$

Therefore, it is trivial to conclude that the mean diameter of the wavy cylinder is equal to D_m , which is unitary by construction. This mean diameter is used as characteristic length in the calculation of flow parameters such as the Reynolds number. Also, it is important to name two special cross sections that will serve as references for comparisons with the straight cylinder, and between the wavy ones: first, the smallest cross section diameter as “Valley”, and second, the largest one as “Peak”.

Table 2 presents the computational costs exclusively referring to the simulation of each case, without considering preliminary simulations to evaluate the domain and mesh resolution.

Table 2. Computational cost.

Case	Time Step	CPU Time (h)
Baseline	7.2×10^{-4}	898
A03	5.4×10^{-4}	1321
A11	1.8×10^{-4}	1980

After the simulation results are generated by Nektar++, mean flow fields and instantaneous force values are mainly processed using both post-processing tools already available in Nektar++ and some in-house scripts written for MATLAB[®]. The in-house scripts assist in processing and plotting the spatial flow field averages over consecutive spanwise wavelengths (given the spatial flow periodicity in this direction), the power spectral density, the graph generation of temporal forces distributions, and coefficients distributions around circumferential positions. Visit, an open-source CFD viewer, is used to visualize the iso-surfaces of the mean streamwise velocity and flow streamlines.

2.5. Mesh Dependence Study

A grid independence study was performed with four different mesh refinements for the smooth cylinder case, by evaluating the convergence of some reference variables (C_d and $C_{l_{RMS}}$). Without loss of generality, the resolution was varied only via h-type refinement, the p-type refinement is the same in all cases, $N_p = 2$. Therefore, the total DOF can be calculated by multiplying N_{Total} by 2^3 . The results in Table 3 exhibited a suitable convergence of such variables, with little difference between the values of the medium grid, currently selected for this work, and the fine grid. After confronting it with experimental and computational results from the literature, as shown in the results section, the selection of the medium grid was considered adequate, and the same resolution was assigned to the wavy cases since the parameters of the wavy geometric modification are relatively small and produce a geometry smoothly close to the straight cylinder.

Table 3. Grid independence study: summary of tested cases with different mesh resolutions. The p-type refinement is the same in all cases, $N_p = 2$. Relative to h-type refinement, N_{x-y} is the number of quadrilateral elements in $x-y$ plane, N_z is the number of divisions in spanwise direction, and N_{Total} is the total number of hexahedral elements.

Case	N_{Total}	N_{x-y}	N_z	C_d	$C_{l_{RMS}}$
Fine	156.080	3902	40	0.939	0.046
Medium	92.832	2901	32	0.946	0.052
Coarse 1	49.024	1532	32	1.054	0.195
Coarse 2	20.944	1309	16	1.054	0.203

3. Results and Discussion

3.1. Numerical Validation

First of all, the results for the straight model, which is the baseline for this study, were compared to those available in the literature in Table 4. We note that our implicit LES results

are closer to the DNS of Beaudan and Moin [50] than to the classic LES of Kravchenko and Moin [51]. The good agreement of these main flow variables serves as a primary validation for the numerical methodology (including the mesh) employed here. Values of lift and drag coefficients over time for the straight case are shown in Figure 7a. The Strouhal number was extracted from the main peak value of the PSD curve, see Figure 8a, calculated from the temporal history of C_l (Figure 7a). The separation angle θ_s was estimated considering the criterion of $C_f = 0$ applied to the curve of skin friction coefficient of the baseline model given in Figure 9.

Table 4. Comparison and validation of results for the straight cylinder at Reynolds 3900.

Author	Nature	Cd	$-C_{pb}$	St	θ_s
Norberg [52]	Experimental	0.98	0.84	0.21	-
Ong and Wallace [53]	Experimental	0.99	-	0.21	86
Lourenco and Shih [54] cited in [50]	Experimental	0.99	0.88	0.22	89
Beaudan and Moin [50]	DNS	0.96	0.89	0.216	85.3
Tremblay [55]	DNS	1.03	0.93	0.215	86.5
Kravchenko and Moin [51]	Classic LES	1.04	0.93	0.21	88
Present work	Implicit LES	0.95	0.84	0.226	86

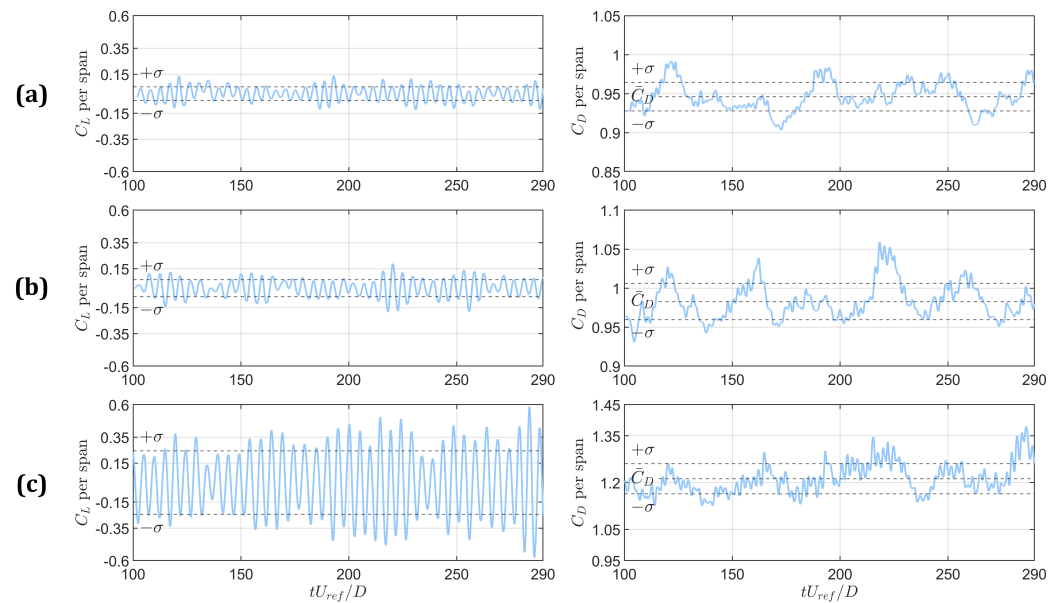


Figure 7. Histories of lift coefficient (left) and drag coefficient (right) for the baseline (a), A03 (b), and A11 (c) models.

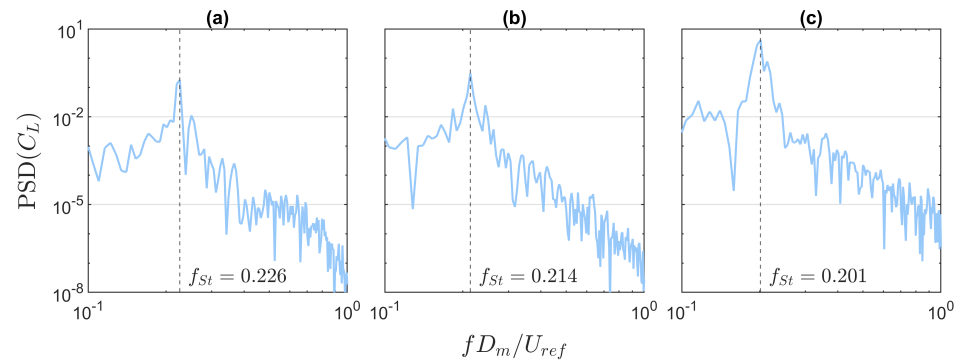


Figure 8. Power spectral density of lift fluctuations for the baseline (a) and wavy cases A03 (b) and A11 (c).

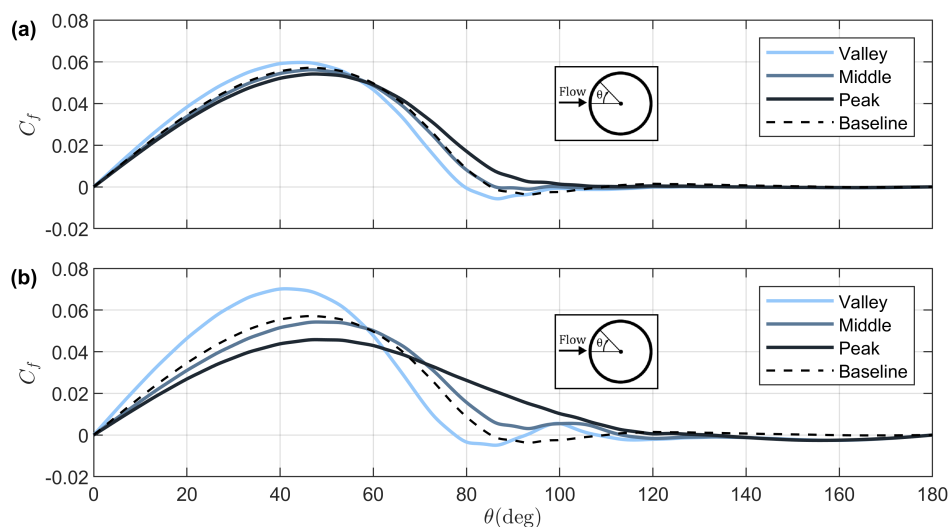


Figure 9. Sectional mean C_f distributions for A03 (a) and A11 (b). A dashed curve denotes the baseline C_f .

In addition, the Cl_{RMS} value, see Table 5, is in the range of typical values found for this Reynolds number, which is around 0.08 for $Re = 3900$ [56]. Nevertheless, this Reynolds number is still reasonably close to the range in which the so-called lift crisis takes place ($260 < Re < 1600$), where Cl_{RMS} has a large behavioral variation, in which Cl_{RMS} values drop dramatically from ≈ 0.5 to 0.045, that is, a more significant variation could be observed. Notwithstanding, as shown in Table 4, all mean values of Cd and Cl_{RMS} are in line with experimental and computational results, as well as the Strouhal number, the separation angle and the base pressure coefficient.

Table 5. Summary of relevant non-dimensional coefficients for the simulated cases.

Case	St	Cl_{RMS}	Cd	Cd Valley	Cd Peak	Cd Middle
Baseline	0.226	0.052	0.946	0.946	0.946	0.946
A03	0.214	0.066	0.983	0.941	1.024	0.977
A11	0.201	0.245	1.212	1.068	1.316	1.184

3.2. Changes in Drag, Lift, and Shedding Frequency

We now turn to discuss how the relevant non-dimensional coefficients change as leading-edge undulation is applied. A summary of these quantities is given in Table 5, featuring the non-dimensional shedding frequency or Strouhal number St , lift coefficient RMS values Cl_{RMS} , the mean overall drag coefficient Cd , and also three sectional (2D) drag coefficients. The latter represent the drag of sections containing a valley, a peak, and those in the middle (for which the diameter matches the original, baseline one). The mean values for the overall drag coefficient and the RMS values of the lift coefficient were obtained from the time histories of these two quantities, which can be seen in Figure 7.

The main effects of leading-edge waviness gathered from Table 5 and Figure 7 are an increase in Cd and Cl_{RMS} , especially for case A11, and a slight decrease in the primary shedding frequency value St . We note that the latter have been evaluated from PSD plots of the lift fluctuation history, which are shown in Figure 8. It is also noteworthy that St values decrease gradually as the undulation amplitude is made larger, whereas the increase in Cd and Cl_{RMS} is more sudden, rising significantly from A03 to A11. This is related to a marked reduction in the base pressure coefficient C_{pb} , as will be discussed below in connection to Figure 10.

As made clear in the introduction, the typical effect of undulation in traditional wavy cylinders is to decrease the mean Cd . In order to help unveil why the opposite is being observed in the case of leading-edge waviness, the surface distributions of friction

coefficient C_f and pressure coefficient C_p is discussed below. These distributions are shown in Figures 9 and 10, respectively.

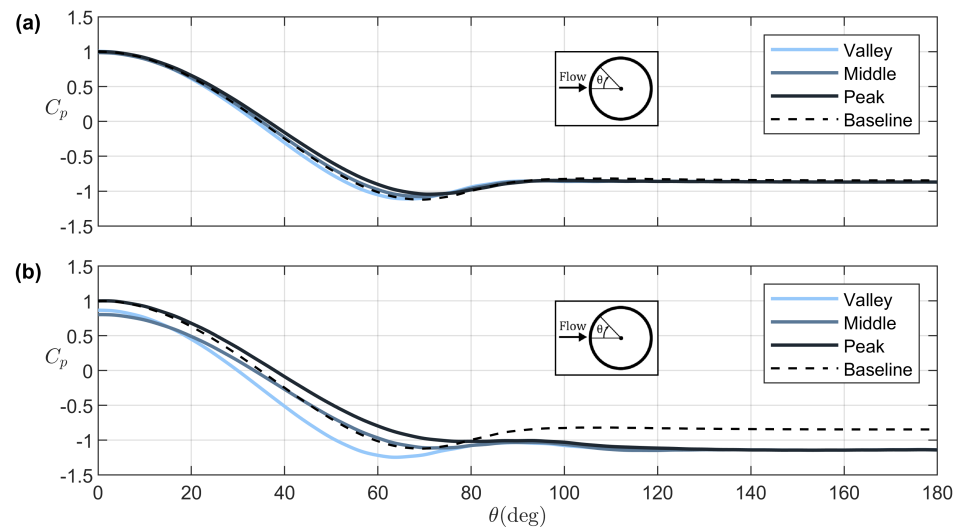


Figure 10. Sectional mean C_p distributions for A03 (a) and A11 (b). A dashed curve denotes the baseline C_p .

The C_f distributions in Figure 9 show that the curves representing middle sections are not much different from the reference C_f curve of the baseline cylinder (dashed). For the other sections (peak and valley), each C_f curve changes in such a symmetrical way that the overall friction drag for those sections is not significantly altered. This indicates that the changes in overall C_d due to undulation are primarily caused by changes in pressure distribution. Still, important information that can be extracted from C_f plots has to do with flow detachment. The mean separation location can be defined from the point in which the C_f curve crosses zero (reversal of velocity profile near the surface). Moreover, the inclination (steepness) of the curve at this point of crossing typically indicates how abrupt the separation is. Hence, by looking at Figure 9, one can conclude that separation is anticipated at valleys and delayed at peaks, these effects being stronger at larger undulation amplitudes. Moreover, it seems that separation at valleys can be rather abrupt (especially for case A11), whereas separation at peaks seems to be much smoother. This is in fact the case, as will be discussed in connection to the iso-surfaces of mean streamwise velocity at near zero value, to be shown later, where vigorous boundary layer detachments are observed when separation occurs at the valleys.

Now, turning to the C_p distributions of Figure 10, one can see why case A03 has no significant change in C_d when compared to the baseline cylinder, namely, there is no significant change in pressure distribution, even along the spanwise direction. However, when it comes to case A11, the situation changes dramatically, especially with regard to the base pressure (C_{pb}) which becomes significantly reduced. This is likely the primary cause for the significant rise in mean C_d for case A11. For some reason, the base pressure seems to follow the pressure at the first location of separation (valley section), whose detachment occurs slightly before $\theta = 80$ degrees, see Figure 9. Curiously, this does not happen with case A03, since a pressure recovery occurs from its first separation location until $\theta \approx 100$ degrees, after which the base pressure remains constant. It seems that for case A11, something takes between $80 < \theta < 100$ that prevents this pressure recovery. This will be further investigated in the next section through the analysis of the coherent structures that form in connection to the separation along valleys.

Lastly, it is worth mentioning that Figure 10 explains why the sectional drag at valleys is smaller than that at peaks, see Table 5. Essentially, undulation decreases the minimum pressure value on the C_p curve of valleys, imparting a suction on the frontal part of the section and therefore reducing its drag. The opposite effect is observed for the C_p

distribution of the peak section, which then contributes the most to the increased overall mean drag C_d . It is believed that the C_p reduction along valleys is caused by a Venturi-like effect due to the constriction of fluid between to peaks.

3.3. Flow Field Analysis and Coherent Structures

We start by looking at two-dimensional plots of mean spanwise vorticity ω_z for the cylinders' three relevant sections, as shown in Figure 11. Note that these plots show the correct size of each cylinder's section, with valleys having smaller diameters and peaks having larger ones — except for the baseline cylinder, whose plots in the top row of Figure 11 are simply repeated for convenience. An important effect of undulation, as discussed in the previous section, is to delay separation at peaks and to anticipate it at valleys. This effect is clearly seen in Figure 11, especially at the bottom row of plots (case A11). In the latter, one can see that the shear layers behind a peak section are closer to one another as they bracket the recirculation region (near wake). They also originate from the cylinder at a greater azimuthal coordinate (separation angle). In contrast, for the valley section, the shear layers detach from the cylinder much earlier, becoming farther away from one another along the recirculation zone. These will visually look like strong “ejection-like” events subsequently to be discussed later. These observations are in line with studies on traditional wavy cylinders, although flow detachment, even when anticipated at valleys, is typically not as strong as the ones found here.

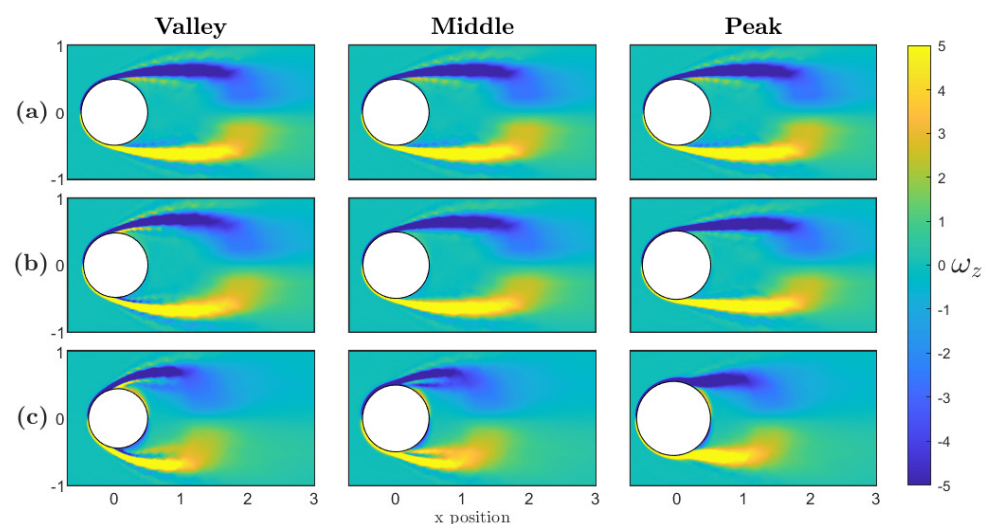


Figure 11. Two-dimensional contours of mean spanwise vorticity ω_z for the three relevant sections (see the header on top) of the simulated cylinders: baseline (a), A03 (b), and A11 (c). The baseline model plots are repeated on the top row.

Another effect observed in Figure 11 is that leading-edge undulation causes the recirculation region at the near wake to reduce its length in the streamwise direction. This effect, nevertheless, is in contrast to studies on traditional wavy cylinders, where the recirculation length typically becomes larger in comparison to that of the straight cylinder. In the literature, an increase in recirculation zone length is normally associated with a reduction in turbulent kinetic energy at the near wake. Here, we found that this trend is followed in the sense that the observed reduction in recirculation zone length leads to an increase in turbulent kinetic energy (TKE), as shown in Figure 12. This figure shows a carpet-like view in the $y = 0$ plane for the three cylinders, whose shapes (cross-sections) appear in white color.

For each cylinder, Figure 12 shows a relatively small TKE variation in the spanwise direction (note each plot repeats itself periodically along the span, following the undulation wavelengths), but it is clear that maximum TKE is reached behind valleys. However, when comparing the cylinders, it becomes clear that leading-edge undulation not only increases

overall TKE levels in the near wake, but also brings the high-TKE zone closer to the cylinder, which is consistent with the reduction in recirculation length. Turbulence along the wake can also be assessed through the energy spectrum of the velocity components, as given in Figure 13, which also shows the pressure spectrum (all these are span-averaged).

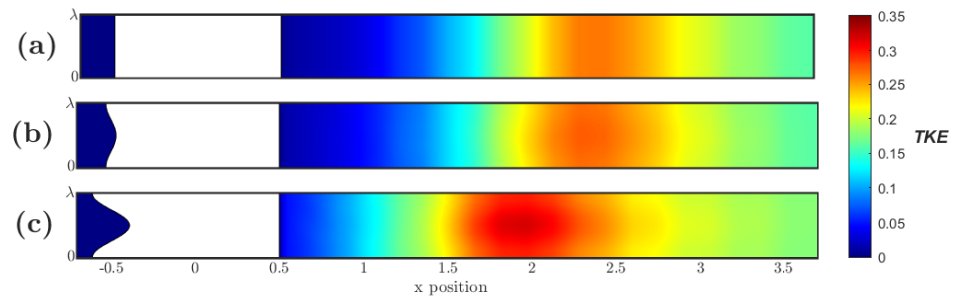


Figure 12. Carpet-like view of mean turbulent kinetic energy in the $y = 0$ plane: baseline (a), A03 (b), and A11 (c). As a spanwise periodic phenomenon, the spatial average referring to the repetition of wavelengths is calculated and exhibited here as a single wavelength.

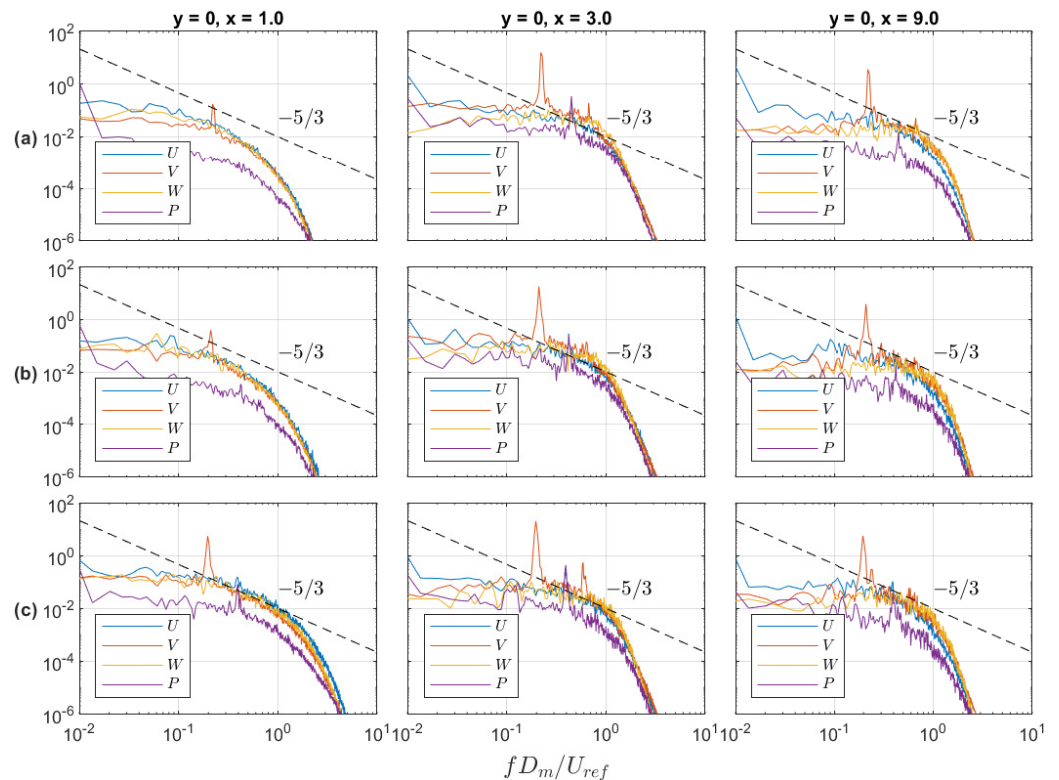


Figure 13. Energy spectrum of velocity components and of pressure at $y = 0$ and different x positions (see top header) for the three simulated cylinders: baseline (a), A03 (b), and A11 (c).

The positions along the wake where the spectra in Figure 13 have been measured can be correlated with the coordinates shown in Figures 11 and 12. Kolmogorov's $-5/3$ slope is included in the plots of Figure 13 for reference and its agreement with the measured spectra over the inertial range of the turbulence cascade further corroborates the suitability of the numerical methodology (including the mesh) employed. The rise in TKE intensity on the near wake due to undulation can be noted by comparing the spectra in the left column of Figure 13, as the curves move upwards from plots (a) to (c). Moreover, note that the peak in the y velocity component (V in the plots) increases especially for case A11 in the near wake, consistent with the rise in Cl_{RMS} discussed in the previous section, see Table 5. This also seems to be related to an anticipation of wake turbulence levels due to undulation, which

can be noted by comparing the spectra of case A11 at $x = 1$ with that of the baseline case at $x = 3$. In this comparison, note that not only the peak in V is anticipated, but also the peak in pressure. This indicates that the turbulent features of the wake are anticipated, which is in line with the recirculation length being reduced. As the more intense turbulent activity is then brought closer to the cylinder, it is not that surprising that stronger oscillations will affect the cylinder, which helps explain at least partially the rise in Cl_{RMS} . In summary, the strong oscillations in y -velocity that would otherwise take place further downstream are now happening at the near wake, affecting the vortex shedding itself in a way that increases oscillations in Cl . Lastly, it is worth noting that the spectra measured at the far wake ($x = 9$) do not change significantly among cylinders, as the turbulent wakes seem to relax toward a canonical turbulent wake state.

Finally, we turn to the analysis of streamwise vorticity, which will reveal the formation of strong (streamwise) vortex pairs associated with how separation is anticipated along valleys and delayed along peaks. In order to track the evolution of said vorticity, we first consider the frontal part of the cylinders by using the azimuthal coordinate θ as a parameter, while looking at the vorticity component ω_t that is tangent to the (circular) cross-sections of the cylinder, as show in Figure 14 (left schematic). Hence, in Figure 15, ω_t will be shown in the r - θ plane that contains the original (baseline) axis of the cylinders, for increasing values of θ . After $\theta = 90$ degrees, i.e., for the rear part of the cylinders, the streamwise vorticity component ω_x will be considered instead, as this will more naturally allow for the tracking of the (streamwise) vortex pairs that, at this point, are no longer attached to the cylinders' surface. Thus, in Figure 16, streamwise vorticity is shown over the y - z plane, with the x coordinate being used as the parameter.

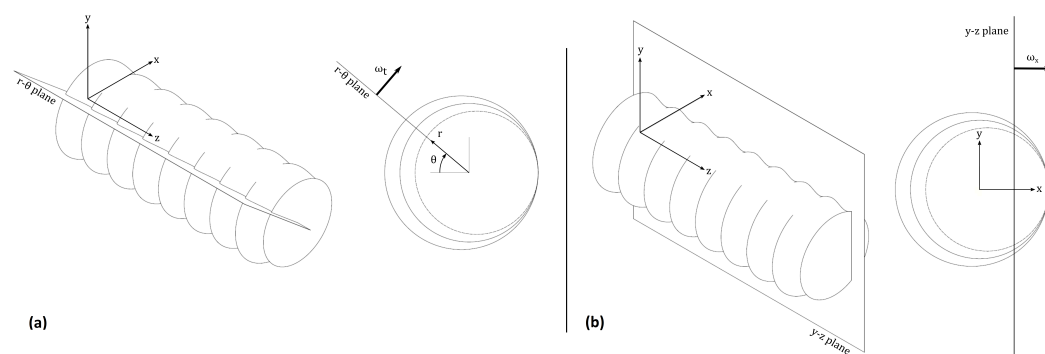


Figure 14. Planes and coordinates chosen to best follow the evolution of vorticity along the surface and after separation: tangent component ω_t for the cylinders' frontal part (a) and streamwise component ω_x for the cylinders' rear part (b).

In Figure 15, ω_t is shown for cases A03 (top) and A11 (bottom) for increasing values of θ . Note that ω_t would be zero for the baseline cylinder (at least for the mean flow) since it represents a distributed vorticity field associated with the boundary layer flow that exists along the spanwise direction (cross-flow) due to surface undulation. For $\theta < 20$ degrees, the plots basically indicate that, with respect to the spanwise direction, the boundary layer evolves from the peaks to the valleys, as expected near the leading-edge region. As θ increases, the direction of flow becomes reversed, as can be seen by how the colors have changed by $\theta = 80$ degrees. This reversal is likely associated with flow separation, which first occurs at valleys around $\theta = 80$ degrees, recall Figure 9. More specifically, the near-surface flow between peaks seems to be accommodating beforehand to bifurcate upon encountering the “ejections-like” by which separation at valleys occurs. These flow structures can be seen in Figure 17 and are surprisingly strong for case A11. Lastly, it is also worth noting in Figure 15 that the vorticity layer near the surface is thicker for case A11, which is likely caused by a stronger cross-flow due to larger undulation amplitude.

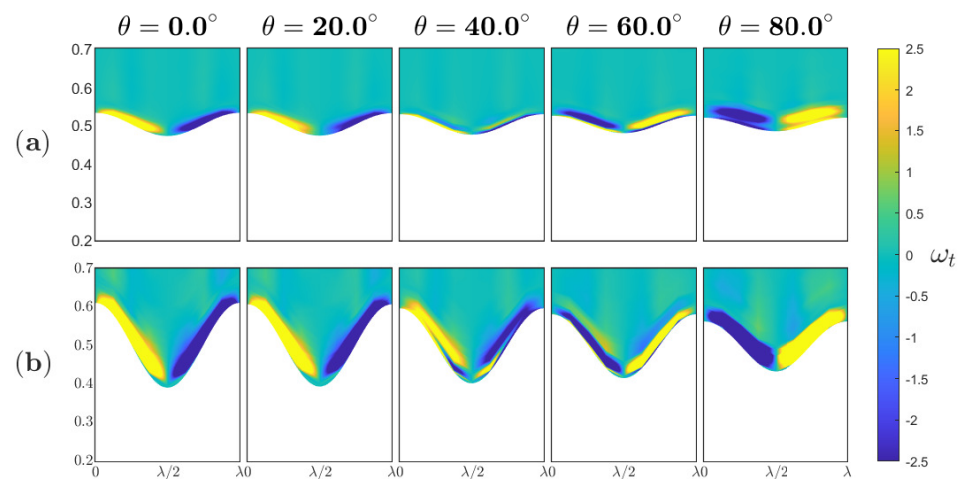


Figure 15. Contours of mean tangent vorticity ω_t over the r - θ plane for the two wavy models, A03 (a) and A11 (b), for increasing values of θ . Refer to Figure 14 (left schematic) for the planes and coordinates adopted. As a spanwise periodic phenomenon, the spatial average referring to the repetition of wavelengths is calculated and exhibited here as a single wavelength.

In Figure 16, it becomes clear that each side of the vorticity layer will, upon flow separation at valleys, detach from the surface and, once free, will roll-up upon itself and become a coherent streamwise vortex. Therefore, the two sides of the vorticity layer between peaks will become a pair of counter-rotating vortices. Globally, the array of undulation wavelengths along the span generates a corresponding array of streamwise vortex pairs. Clearly, from Figure 16, case A11 features much stronger vortices than case A03, as expected from the overall amount of streamwise vorticity held in the respective vorticity layers prior to separation (recall comment at the end of the previous paragraph). The right-most pair of plots in Figure 16 correspond to the plane $x = 0.5$, which is the one containing the trailing edge of the cylinders. At this point, the vortices of case A03 are already vanishing, whereas those of case A11 are still strong and will surely extend further into the near wake region. This will be made more evident in Figure 18, in which streamlines are employed to highlight the coherent pair of streamwise vortices. In fact, as per Figure 18, the vortices of case A03 are not strong enough to produce a cyclical streamline swirl, indicating that only case A11 effectively produces coherent vortices.

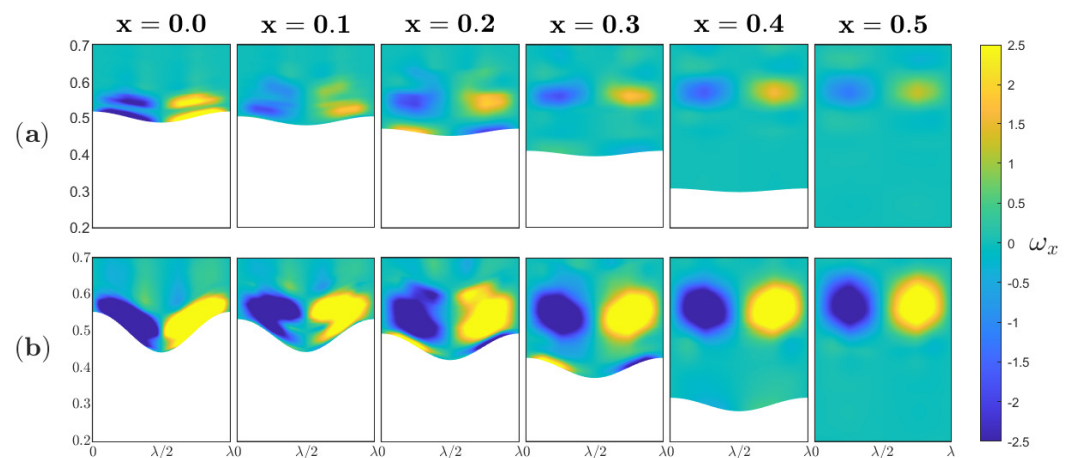


Figure 16. Contours of mean streamwise vorticity ω_x over the y - z plane for the wavy models, A03 (a) and A11 (b), for increasing values of x . Refer to Figure 14 (right schematic) for the planes and coordinates adopted. As a spanwise periodic phenomenon, the spatial average referring to the repetition of wavelengths is calculated and exhibited here as a single wavelength.

In Figure 17, iso-surfaces of mean streamwise velocity at a near zero value ($U \leq 10^{-3}$) are employed to highlight how the flow separation takes place for each cylinder. One can clearly see how separation first occurs at valleys by means of separated vortical shear layers of fluid moving away from the surface. These can be connected to the streamwise vortices by correlating Figure 17 to Figure 16. The vortex pair between two peaks rotates in such a way as to “lift” fluid from the surface at valleys and to “land” fluid on the surface at peaks. The former of these effects explains why such structures are stronger when vortices are stronger, whereas the latter explains why separation at peaks is further delayed when vortices are stronger, recall Figure 9.

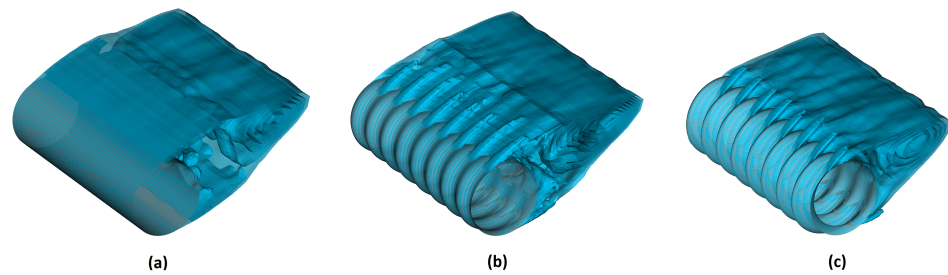


Figure 17. Iso-surfaces of mean streamwise velocity at a near zero value ($U \leq 10^{-3}$), showing how the flow separation at valleys occurs by means of “ejections-like” events. The three simulated cylinders are shown: baseline (a), A03 (b) and A11 (c).

In Figure 18, streamlines based on the mean flow are used to highlight the formation of the coherent vortices. They clearly show that only case A11 produces vortices that are effectively cyclical. The left-most figure of case A11 in Figure 18 shows how the vortex pair adjacent to a peak pushes out fluid toward the surface. Since this happens prior to separation at peaks, the overall velocity increases in this region, and, therefore, pressure is reduced (Bernoulli equation). This is consistent with the C_p curve along peaks already shown (see Figure 10 for $80 < \theta < 120$ degrees). Hence, when separation occurs at peaks, the pressure at the surface is significantly reduced. This, combined with the fact that the earlier separation at valleys also happened at a location of reduced pressure ($\theta_s \approx 80$ degrees), ends up allowing for reduced pressure on the separation zone and near wake. In summary, the mechanism proposed to explain the increased drag of case A11 due to low base pressure is that strong coherent vortices increase the overall velocity just before separation at peaks, leading to reduced pressure on the separation zone.

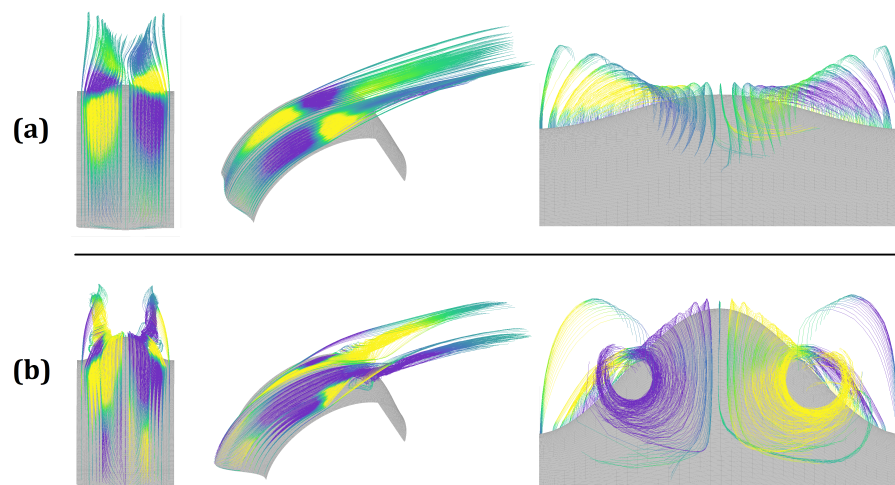


Figure 18. Mean flow-based streamlines showing the formation of coherent streamwise vortices for the wavy cylinders: A03 (a) and A11 (b). Only case A11 produces effectively complete cyclical vortices. The colors indicate local streamwise vorticity.

4. Conclusions

We presented a numerical study on the flow past cylinders with leading-edge waviness. This type of waviness resembles the tubercles found on the flippers of humpback whales and has been often studied in the context of wavy wings. To the authors' knowledge, this was the first study to consider this type of waviness for cylinders, since traditional studies on wavy cylinders typically apply undulation both to leading and trailing edges.

Some of the results obtained here were similar to those of traditional wavy cylinders, such as anticipated separation at valleys (sections with smaller diameters) and delayed at peaks (sections with larger diameters). Still, most flow changes affected by leading-edge undulation were found to be in contrast to those observed in traditional wavy cylinders. An explanation for these unexpected effects was then proposed based on a detailed flow field analysis. Specifically, the formation of counter-rotating streamwise coherent vortices was correlated to the delay of separation along peaks. Those vortices seem to push outer fluid toward the surface prior to separation at peaks, increasing overall velocity and reducing the pressure right before separation, especially for case A11. This defined a significantly lower base pressure (up to about 36%) and caused the observed rise in drag (up to about 28%). This decrease in base pressure likely draws the near wake features closer to the cylinder, for example, by reducing the recirculation length. Since the turbulent structures of the near wake become more "compressed" closer to the cylinder—compared to the straight cylinder, the turbulent kinetic energy rises on the near wake and the larger oscillations in y -velocity of the vortex formation zone impart larger oscillations in the lift. As all these combined effects are far from simple, subsequent studies could further clarify the underlying dynamics.

It seems that the most relevant aspect in the reduction of base pressure is the strength of the coherent streamwise vortices. Their strength is nevertheless related to undulation (wavelength and amplitude), as well as to the Reynolds number. It is worth mentioning that an experimental study currently being conducted on similar geometries, see [13], but at much larger Reynolds numbers, showed a reduction in drag instead, which confirms its Reynolds number dependence.

Although the results did not replicate the feats of the wavy airfoil or even the typical wavy cylinders, this study was able to offer a good phenomenological description that may be useful in understanding and complementing these other studies. Furthermore, a practical application for it beyond flow control mechanisms, by taking advantage of the observed mixing layer effect promoted by the streamwise vortices, would be in circular tubes of heat exchangers. Additionally, more studies are being conducted to explore the possibilities of this geometric modification to different parameters combinations.

Author Contributions: Conceptualization, P.H.F., T.B.d.A. and R.C.M.; methodology, P.H.F. and R.C.M.; software, P.H.F., E.O.C. and L.D.F.; validation, P.H.F. and R.C.M.; formal analysis, P.H.F., T.B.d.A., E.O.C., L.D.F. and R.C.M.; investigation, P.H.F., T.B.d.A. and R.C.M.; data curation, P.H.F.; writing—original draft preparation, P.H.F. and R.C.M.; writing—review and editing, P.H.F.; visualization, P.H.F., E.O.C. and L.D.F.; supervision, R.C.M. and T.B.d.A.; funding acquisition, R.C.M. All authors have read and agreed to the published version of the manuscript.

Funding: This research was funded by FAPESP grant number 2020/10910-8. The APC was funded by CNPq (process number 141783/2019-2).

Data Availability Statement: Not applicable.

Acknowledgments: The authors would like to thank André F. C. da Silva and Mohsen Lahooti for their support regarding the efficient use of Nektar++ in the context of parallel computations. In addition, the first author acknowledges support from CNPq for his Ph.D. scholarship (process number 141783/2019-2).

Conflicts of Interest: The authors declare no conflict of interest.

References

1. Roshko, A. Perspectives on bluff body aerodynamics. *J. Wind Eng. Ind. Aerodyn.* **1993**, *49*, 79–100. [[CrossRef](#)]
2. Williamson, C.H.K. Three-dimensional wake transition. *J. Fluid Mech.* **1996**, *328*, 345–407. [[CrossRef](#)]
3. Zdravkovich, M.M. *Flow Around Circular Cylinders—Fundamentals*; Oxford University Press: Oxford, UK, 1997; Volume 1.
4. Bearman, P.W. Vortex Shedding from Oscillating Bluff Bodies. *Annu. Rev. Fluid Mech.* **1984**, *16*, 195–222. [[CrossRef](#)]
5. Wang, R.; Xin, D.; Ou, J. Experimental investigation on suppressing circular cylinder VIV by a flow control method based on passive vortex generators. *J. Wind Eng. Ind. Aerodyn.* **2019**, *187*, 36–47. [[CrossRef](#)]
6. Fish, F.E.; Battle, J.M. Hydrodynamic design of the humpback whale flipper. *J. Morphol.* **1995**, *225*, 51–60. [[CrossRef](#)]
7. Miklosovic, D.S.; Murray, M.M.; Howle, L.E.; Fish, F.E. Leading-edge tubercles delay stall on humpback whale (*Megaptera novaeangliae*) flippers. *Phys. Fluids* **2004**, *16*, L39–L42. [[CrossRef](#)]
8. Johari, H.; Henocho, C.; Custodio, D.; Levshin, A. Effects of leading-edge protuberances on airfoil performance. *AIAA J.* **2007**, *45*, 2634–2642. [[CrossRef](#)]
9. Hansen, K.; Kelso, R.; Dally, B. The effect of leading edge tubercle geometry on the performance of different airfoils. In Proceedings of the 7th World Conference on Experimental Heat Transfer, Fluid Mechanics and Thermodynamics, Krakow, Poland, 28 June–3 July 2009.
10. de Paula, A.A.; Meneghini, J.; Kleine, V.G.; Girardi, R.D. The wavy leading edge performance for a very thick airfoil. In Proceedings of the 55th AIAA Aerospace Sciences Meeting, Grapevine, TX, USA, 9–13 January 2017.
11. Rocha, F.A.; de Paula, A.A.; de Sousa, M.; Cavalieri, A.V.; Kleine, V.G. Lift enhancement by wavy leading edges at Reynolds numbers between 700,000 and 3,000,000. In Proceedings of the 36th AIAA Applied Aerodynamics Conference, Atlanta, GA, USA, 25–29 June 2018.
12. Seyhan, M.; Sarioglu, M.; Akansu, Y.E. Influence of Leading-Edge Tubercle with Amplitude Modulation on NACA 0015 Airfoil. *AIAA J.* **2021**, *59*, 3965–3978. [[CrossRef](#)]
13. Ferreira, P.H.; Moura, R.C.; de Araújo, T.B. Experimental Investigation of a Wavy Leading Edge Cylinder. In Proceedings of the AIAA Aviation 2022 Forum, Chicago, IL, USA, 27 June–1 July 2022.
14. Ahmed, A.; Bays-Muchmore, B. Transverse flow over a wavy cylinder. *Phys. Fluids A Fluid Dyn.* **1992**, *4*, 1959–1967. [[CrossRef](#)]
15. Zhang, W.; Daichin; Lee, S.J. PIV measurements of the near-wake behind a sinusoidal cylinder. *Exp. Fluids* **2005**, *38*, 824–832. [[CrossRef](#)]
16. Lam, K.; Lin, Y.F. Large eddy simulation of flow around wavy cylinders at a subcritical Reynolds number. *Int. J. Heat Fluid Flow* **2008**, *29*, 1071–1088. [[CrossRef](#)]
17. Lin, Z.; Yu-feng, L. Force reduction of flow around a sinusoidal wavy cylinder. *J. Hydrodyn. Ser. B* **2009**, *21*, 57–96.
18. Lam, K.; Lin, Y.F.; Zou, L.; Liu, Y. Investigation of turbulent flow past a yawed wavy cylinder. *J. Fluids Struct.* **2010**, *26*, 1078–1097. [[CrossRef](#)]
19. Zhao, R.; Xu, J.; Yan, C.; Yu, J. Scale-adaptive simulation of flow past wavy cylinders at a subcritical Reynolds number. *Acta Mech. Sin.* **2011**, *27*, 660–667. [[CrossRef](#)]
20. Bai, H.L.; Zang, B.; New, T.H. The near wake of a sinusoidal wavy cylinder with a large spanwise wavelength using time-resolved particle image velocimetry. *Exp. Fluids* **2019**, *60*, 15. [[CrossRef](#)]
21. Karthik, K.; Jeyakumar, S.; Sebastin, J.S. Optimization of wavy cylinder for aerodynamic drag and aeroacoustic sound reduction using computational fluid dynamics analysis. *Proc. Inst. Mech. Eng. Part C J. Mech. Eng. Sci.* **2021**, *235*, 1–13. [[CrossRef](#)]
22. Zhang, Z.; Tu, J.; Zhang, K.; Yang, H.; Han, Z.; Zhou, D.; Xu, J.; Zhang, M. Vortex characteristics and flow-induced forces of the wavy cylinder at a subcritical Reynolds number. *Ocean Eng.* **2021**, *222*, 108593. [[CrossRef](#)]
23. Moura, R.C. On the Use of Spectral Element Methods for Under-Resolved Simulations of Transitional and Turbulent Flows. Ph.D. Thesis, Imperial College London, London, UK, 2017.
24. Moura, R.C.; Mengaldo, G.; Peiró, J.; Sherwin, S.J. On the eddy-resolving capability of high-order discontinuous Galerkin approaches to implicit LES/under-resolved DNS of Euler turbulence. *J. Comput. Phys.* **2017**, *330*, 615–623. [[CrossRef](#)]
25. Moura, R.C.; Sherwin, S.J.; Peiró, J. Linear dispersion-diffusion analysis and its application to under-resolved turbulence simulations using discontinuous Galerkin spectral/hp methods. *J. Comput. Phys.* **2015**, *298*, 695–710. [[CrossRef](#)]
26. Moura, R.C.; Sherwin, S.J.; Peiró, J. Modified equation analysis for the discontinuous Galerkin formulation. In *Spectral and High Order Methods for Partial Differential Equations—ICOSAHOM 2014*; Springer: Cham, Switzerland, 2015; pp. 375–383.
27. Moura, R.C.; Sherwin, S.J.; Peiró, J. Eigensolution analysis of spectral/hp continuous Galerkin approximations to advection-diffusion problems: Insights into spectral vanishing viscosity. *J. Comput. Phys.* **2016**, *307*, 401–422. [[CrossRef](#)]
28. Moura, R.C.; Mengaldo, G.; Peiró, J.; Sherwin, S.J. An LES setting for DG-based implicit LES with insights on dissipation and robustness. In Proceedings of the 11th International Conference on Spectral and High Order Methods (under review), Rio de Janeiro, Brazil, 27 June–1 July 2016.
29. Mengaldo, G.; Moura, R.C.; Giralda, B.; Peiró, J.; Sherwin, S.J. Spatial eigensolution analysis of discontinuous Galerkin schemes with practical insights for under-resolved computations and implicit LES. *Comput. Fluids* **2017**, *169*, 349–364. [[CrossRef](#)]
30. Moura, R.C.; Peiró, J.; Sherwin, S.J. On the accuracy and robustness of implicit LES/under-resolved DNS approaches based on spectral element methods. In Proceedings of the 10th International Symposium on Turbulence and Shear Flow Phenomena, Chicago, IL, USA, 7–9 July 2017.

31. Mengaldo, G.; De Grazia, D.; Moura, R.C.; Sherwin, S.J. Spatial eigensolution analysis of energy-stable flux reconstruction schemes and influence of the numerical flux on accuracy and robustness. *J. Comput. Phys.* **2018**, *358*, 1–20. [[CrossRef](#)]
32. Fernandez, P.; Moura, R.C.; Mengaldo, G.; Peraire, J. Non-modal analysis of spectral element methods: Towards accurate and robust large-eddy simulations. *Comput. Method. Appl. M.* **2019**, *346*, 43–62. [[CrossRef](#)]
33. Moura, R.C.; Peiró, J.; Sherwin, S.J. Implicit LES approaches via discontinuous Galerkin methods at very large Reynolds. In *Direct and Large-Eddy Simulation XI*; Springer: Cham, Switzerland, 2019; pp. 53–59.
34. Moura, R.C.; Peiró, J.; Sherwin, S.J. Under-resolved DNS of non-trivial turbulent boundary layers via spectral/hp CG schemes. In *Direct and Large Eddy Simulation XII*; Springer: Cham, Switzerland, 2020; pp. 389–395.
35. Moura, R.C.; Fernandez, P.; Mengaldo, G.; Sherwin, S.J. Viscous diffusion effects in the eigenanalysis of (hybridisable) DG methods. In *Spectral and High Order Methods for Partial Differential Equations ICOSAHOM 2018*; Springer: Cham, Switzerland, 2020; pp. 371–382.
36. Moura, R.C.; Fernandes, L.D.; Silva, A.F.C.; Mengaldo, G.; Sherwin, S.J. Spectral/hp element methods' linear mechanism of (apparent) energy transfer in Fourier space: Insights into dispersion analysis for implicit LES. *J. Comput. Phys.* **2022**, *471*, 111613. [[CrossRef](#)]
37. Martins, Y.W.G.; Malatesta, V.; Moura, R.C. Numerical study of the flow past an inclined flat plate via spectral/hp element methods with novel stabilization. In Proceedings of the 26th International Congress of Mechanical Engineering, Virtual Event, Brazil, 22–26 November 2021.
38. Moura, R.C.; Cassinelli, A.; da Silva, A.F.C.; Burman, E.; Sherwin, S.J. Gradient jump penalty stabilisation of spectral/hp element discretisation for under-resolved turbulence simulations. *Comput. Methods Appl. Mech. Eng.* **2022**, *388*, 114200. [[CrossRef](#)]
39. Moura, R.C.; Aman, M.; Peiró, J.; Sherwin, S.J. Spatial eigenanalysis of spectral/hp continuous Galerkin schemes and their stabilisation via DG-mimicking spectral vanishing viscosity: Application to high Reynolds number flows. *J. Comput. Phys.* **2019**, *406*, 109112. [[CrossRef](#)]
40. Cantwell, C.D.; Moxey, D.; Comerford, A.; Bolis, A.; Rocco, G.; Mengaldo, G.; de Grazia, D.; Yakovlev, S.; Lombard, J.; Ekelschot, D.; et al. Nektar++: An open-source spectral/hp element framework. *Comput. Phys. Commun.* **2015**, *192*, 205–219. [[CrossRef](#)]
41. Moxey, D.; Cantwell, C.D.; Bao, Y.; Cassinelli, A.; Castiglioni, G.; Chun, S.; Juda, E.; Kazemi, E.; Lackhove, K.; Marcon, J.; et al. Nektar++: Enhancing the capability and application of high-fidelity spectral/hp element methods. *Comput. Phys. Commun.* **2020**, *249*, 1–18. [[CrossRef](#)]
42. Lombard, J.W.; Moxey, D.; Sherwin, S.J.; Hoessler, J.F.A.; Dhandapani, S.; Taylor, M.J. Implicit large-eddy simulation of a wingtip vortex. *AIAA J.* **2016**, *54*, 506–518. [[CrossRef](#)]
43. Serson, D.; Meneghini, J.R.; Sherwin, S.J. Direct numerical simulations of the flow around wings with spanwise waviness. *J. Fluid Mech.* **2017**, *826*, 714–731. [[CrossRef](#)]
44. Wang, R.; Wu, F.; Xu, H.; Sherwin, S.J. Implicit large-eddy simulations of turbulent flow in a channel via spectral/hp element methods. *Phys. Fluids* **2021**, *33*, 035130. [[CrossRef](#)]
45. Mengaldo, G.; Moxey, D.; Turner, M.; Moura, R.C.; Jassim, A.; Taylor, M.; Peiro, J.; Sherwin, S.J. Industry-relevant implicit large-eddy simulation of a high-performance road car via spectral/hp element methods. *SIAM Rev.* **2021**, *63*, 723–755. [[CrossRef](#)]
46. Karniadakis, G.; Sherwin, S.J. *Spectral/hp Element Methods for Computational Fluid Dynamics*; Oxford University Press: Oxford, UK, 2005.
47. Raza, S.A.; Irawan, Y.H.; Chern, M. Effect of boundary conditions and domain size on the turbulent flow characteristics over a circular cylinder. *J. Chin. Inst. Eng.* **2021**, *44*, 659–672. [[CrossRef](#)]
48. Ali, H.; Khan, N.B.; Jameel, M.; Khan, A.; Sajid, M.; Munir, A.; Ahmed, A.E.; Alharbi, K.A.M.; Galal, A.M. Numerical investigation of the effect of spanwise length and mesh density on flow around cylinder at $Re = 3900$ using LES model. *PLoS ONE* **2022**, *17*, e0266065. [[CrossRef](#)] [[PubMed](#)]
49. Geuzaine, C.; Remacle, J.F. Gmsh: A three-dimensional finite element mesh generator with built-in pre- and post-processing facilities. *Int. J. Numer. Methods Eng.* **2009**, *79*, 1309–1331. [[CrossRef](#)]
50. Beaudan, P.; Moin, P. *Numerical Experiments on the Flow Past a Circular Cylinder at Sub-Critical Reynolds Number*; Technical Report No. TF-62; Thermosciences Division, Department of Mechanical Engineering, Stanford University: Stanford, CA, USA, 1994.
51. Kravchenko, A.G.; Moin, P. Numerical studies of flow over a circular cylinder at $Re = 3900$. *Phys. Fluids* **2000**, *12*, 403–417. [[CrossRef](#)]
52. Norberg, C. *Effects of Reynolds Number and a Low-Intensity Freestream Turbulence on the Flow around a Circular Cylinder*; Technical Report Publication 87/2; Department of Applied Thermodynamics and Fluid Mechanics, Chalmers University of Technology: Gothenburg, Sweden, 1987.
53. Ong, L.; Wallace, J.M. The velocity field of the turbulent very near wake of a circular cylinder. *Exp. Fluids* **1996**, *20*, 441–453. [[CrossRef](#)]
54. Lourenco, L.M.; Shih, C. Characteristics of the Plane Turbulent Near Wake of a Circular Cylinder. A Particle Image Velocimetry Study. *Engineering* **1993**.
55. Tremblay, F. Direct and Large-Eddy Simulation of Flow around a Circular Cylinder at Subcritical Reynolds Numbers. Ph.D. Thesis, Technische Universität München (TUM), Munich, Germany, 2002.
56. Norberg, C. Fluctuating lift on a circular cylinder: Review and new measurements. *J. Fluids Struct.* **2003**, *17*, 57–96. [[CrossRef](#)]